

Quantitative Methods to Investigate the 4D Dynamics of Heterochromatic Repair Sites in *Drosophila* Cells

Christopher P. Caridi, Laetitia Delabaere, Harianto Tjong²,
Hannah Hopp³, Devika Das⁴, Frank Alber, Irene Chiolo¹

University of Southern California, Los Angeles, CA, United States

¹Corresponding author: e-mail address: chiolo@usc.edu

Contents

1. Nuclear Dynamics Play Critical Roles in Heterochromatin Repair and Genome Stability	360
2. Methods	366
2.1 Live-Cell Imaging of <i>Drosophila</i> Cells	366
2.2 Image Processing and Focus Tracking	375
2.3 Analysis of Focus Dynamics	379
Acknowledgments	383
Disclosures	383
References	384

Abstract

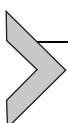
Heterochromatin is mostly composed of long stretches of repeated DNA sequences prone to ectopic recombination during double-strand break (DSB) repair. In *Drosophila*, “safe” homologous recombination (HR) repair of heterochromatic DSBs relies on a striking relocation of repair sites to the nuclear periphery. Central to understanding heterochromatin repair is the ability to investigate the 4D dynamics (movement in space and time) of repair sites. A specific challenge of these studies is preventing phototoxicity and photobleaching effects while imaging the sample over long periods of time, and with sufficient time points and Z-stacks to track repair foci over time. Here we describe an optimized approach for high-resolution live imaging of heterochromatic DSBs in *Drosophila* cells, with a specific emphasis on the fluorescent markers and imaging setup

² Present address: The Jackson Laboratory, Farmington, CT, United States.

³ Present address: Keck School of Medicine, University of Southern California, Los Angeles, CA, United States.

⁴ Present address: Mayo Clinic School of Medicine, AZ, United States.

used to capture the motion of repair foci over long-time periods. We detail approaches that minimize photobleaching and phototoxicity with a DeltaVision widefield deconvolution microscope, and image processing techniques for signal recovery post-imaging using SoftWorX and Imaris software. We present a method to derive mean square displacement curves revealing some of the biophysical properties of the motion. Finally, we describe a method in R to identify tracts of directed motions (DMs) in mixed trajectories. These approaches enable a deeper understanding of the mechanisms of heterochromatin dynamics and genome stability in the three-dimensional context of the nucleus and have broad applicability in the field of nuclear dynamics.



1. NUCLEAR DYNAMICS PLAY CRITICAL ROLES IN HETEROCHROMATIN REPAIR AND GENOME STABILITY

Double-strand breaks (DSBs) in pericentromeric heterochromatin (hereafter, “heterochromatin”) are a major threat to genome stability (recently reviewed in [Amaral, Ryu, Li, & Chiolo, 2017](#); [Caridi, Delabaere, Zapotoczny, & Chiolo, 2017](#); [Chiolo, Tang, Georgescu, & Costes, 2013](#)). Heterochromatin comprises ~30% of fly and human genomes ([Ho et al., 2014](#); [Hoskins et al., 2007, 2015](#); Fig. 1A) and is mostly composed of repeated sequences prone to ectopic recombination during DNA repair ([Amaral et al., 2017](#); [Caridi et al., 2017](#); [Chiolo et al., 2013](#); [Peng & Karpen, 2008](#)). In *Drosophila*, for example, about half of these sequences consist of simple “satellite” repeats (mostly tandem 5-base pair sequences) repeated for hundreds of kilobases to megabases, while the rest are mostly composed of scrambled clusters of transposable elements and about 250 isolated genes ([Ho et al., 2014](#); [Hoskins et al., 2007, 2015](#)). While heterochromatin is a major component of the genome in multicellular eukaryotes, it is absent in budding yeast.

Despite the risk of aberrant recombination, homologous recombination (HR) is largely utilized for repairing heterochromatic DSBs in both flies ([Chiolo et al., 2011](#); [Janssen et al., 2016](#); [Ryu, Bonner, & Chiolo, 2016](#); [Ryu et al., 2015](#)) and mammalian cells ([Beucher et al., 2009](#); [Tsuroula et al., 2016](#)), and studies from our lab and others identified specialized pathways that promote heterochromatin repair while preventing aberrant recombination (reviewed in [Amaral et al., 2017](#); [Caridi et al., 2017](#); [Chiolo et al., 2013](#)). Working with *Drosophila* cells, we discovered that “safe” HR repair relies on a striking relocation of heterochromatic repair sites to the nuclear periphery ([Caridi et al., 2018](#); [Chiolo et al., 2011](#); [Ryu et al., 2016, 2015](#)). Repair starts inside the heterochromatin domain—a

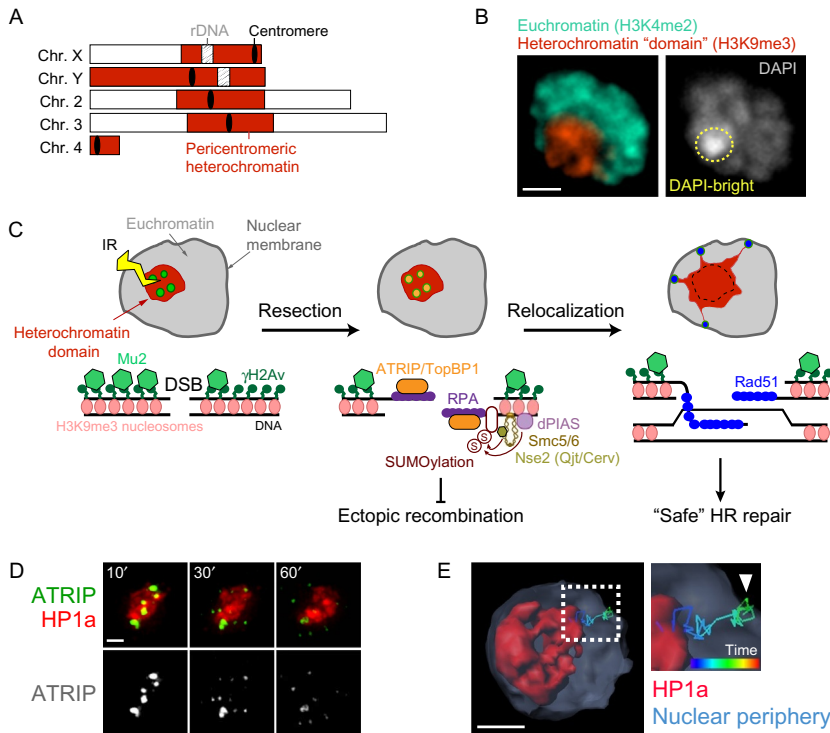


Fig. 1 Nuclear dynamics of heterochromatin repair mechanisms in *Drosophila* cells. (A) Schematic view of *Drosophila* chromosomes showing the position and extent of pericentromeric heterochromatin. (B) Immunofluorescence of a Kc cell showing heterochromatin organized as one distinct domain (red, H3K9me3) comprising the DAPI bright region (yellow circle). Euchromatin surrounds the heterochromatin domain (green, H3K4me2). Scale bar = 1 μ m. (C) HR repair of heterochromatic DSBs starts inside the domain with H2Av phosphorylation and Mu2/Mdc1 recruitment. Resection also occurs inside the domain resulting in ATRIP and TopBP1 foci. Next, the heterochromatin domain expands and repair foci relocalize to the nuclear periphery to form Rad51 foci and continue HR. dPIAS, Nse2/Qjt, and Nse2/Cerv SUMO-ligases are required to block HR progression in the domain and prevent ectopic recombination. (D) Live imaging of one Kc cell expressing mCh-HP1a and EGFP-ATRIP shows ATRIP foci inside the heterochromatin domain at 10 min after IR, which leave the domain by 60 min after IR (Chiolo et al., 2011). (E) 4D reconstruction of one nucleus of a Kc cell expressing mCh-HP1a, mCh-LaminC, and GFP-ATRIP and, exposed to IR, shows an example of a heterochromatic repair focus that leaves the heterochromatin domain and reaches the nuclear periphery (Ryu et al., 2015).

distinct nuclear structure in flies (Chiolo et al., 2011; Riddle et al., 2011; Ryu et al., 2016, 2015; Fig. 1B)—and is temporarily halted after resection and ATRIP/TopBP1 focus formation (Chiolo et al., 2011; Ryu et al., 2016, 2015; Fig. 1C). This block to HR progression is mediated by SUMOylation

via the SUMO E3 ligases dPIAS and Smc5/6 subunits Nse2/Qjt and Nse2/Cerv (Chiolo et al., 2011; Ryu et al., 2016, 2015; Fig. 1C). Next, the heterochromatin domain expands during relocalization (Chiolo et al., 2011). This likely reflects a global relaxation of the chromatin and facilitates damage signaling and/or nuclear dynamics. Repair continues with Rad51 recruitment at the nuclear periphery (Chiolo et al., 2011; Delabaere & Chiolo, 2016; Ryu et al., 2015; Fig. 1D), revealing a tight regulation of repair progression in space and time. Inactivating the relocalization pathway leads to aberrant recombination between heterochromatic sequences, chromosomal aberrations, and heterochromatin instability (Caridi et al., 2018; Chiolo et al., 2011; Ryu et al., 2016, 2015), revealing the importance of these dynamics for genome integrity. In mouse cells, where heterochromatin is organized in several “chromocenters,” these domains expand during repair (Ayoub, Jeyasekharan, Bernal, & Venkitaraman, 2008; Burgess, Burman, Kruhlak, & Misteli, 2014; Tsouroula et al., 2016) and repair sites leave the domains before Rad51 recruitment and HR progression (Chiolo et al., 2013; Jakob et al., 2011; Tsouroula et al., 2016). These observations suggest highly conserved strategies for “safe” heterochromatin repair. Relocalization likely prevents ectopic recombination by isolating the damaged site and its homologous sequences (on the homologous chromosome or the sister chromatid) away from similar sequences on ectopic chromosomes, before strand invasion (Amaral et al., 2017; Caridi et al., 2017; Chiolo et al., 2011, 2013; Ryu et al., 2016, 2015).

In addition, a major body of work in yeast and mammalian cells revealed the dynamic nature of chromatin in both damaged and undamaged regions (reviewed in Amaral et al., 2017; Caridi et al., 2017). Repair sites are highly dynamic during homology search for HR repair (Cho, Dilley, Lampson, & Greenberg, 2014; Dion, Kalck, Horigome, Towbin, & Gasser, 2012; Miné-Hattab & Rothstein, 2012; Neumann et al., 2012; Saad et al., 2014) or during relocalization of relatively rare classes of DSBs to specific subnuclear compartments. For example, DSBs induced in rDNA of yeast and human cells leave the nucleolus during repair (Torres-Rosell et al., 2007; van Sluis & McStay, 2015). Further, persistent DSBs, eroded telomeres, subtelomeric breaks, and collapsed forks relocalize to the nuclear periphery for repair (Chung et al., 2015; Churikov et al., 2016; Horigome et al., 2014, 2016; Kalocsay, Hiller, & Jentsch, 2009; Khadaroo et al., 2009; Nagai et al., 2008; Oza, Jaspersen, Miele, Dekker, & Peterson, 2009; Su, Dion, Gasser, & Freudenreich, 2015; Swartz, Rodriguez, & King, 2014; Therizols et al., 2006; recently reviewed in Amaral et al., 2017; Caridi et al., 2017). Interestingly, SUMOylation appears to drive the relocalization

of repair sites in different contexts, revealing conserved pathways for the regulation of nuclear dynamics during DSB repair (Churikov et al., 2016; Horigome et al., 2016; Kalocsay et al., 2009; Khadaroo et al., 2009; Nagai et al., 2008; Oza et al., 2009; Su et al., 2015; Torres-Rosell et al., 2007). Structural components in the cytoplasm appear to influence nuclear dynamics via SUN–KASH protein complexes traversing the nuclear membrane (Lottersberger, Karssemeijer, Dimitrova, & de Lange, 2015; Spichal et al., 2016). In addition, the entire genome becomes more dynamic in response to DSBs, albeit to a lesser extent relative to repair sites (Krawczyk et al., 2012; Lottersberger et al., 2015; Miné-Hattab & Rothstein, 2012; Seeber, Dion, & Gasser, 2013). This global mobilization of the genome correlates with increased susceptibility to micrococcal nucleic acid digestion in response to DSB induction (Ziv et al., 2006) and possibly results from a global decrease in histone levels following DNA damage (Hauer et al., 2017; Kruhlak et al., 2006), release of chromatin-associated components (Ziv et al., 2006), or loss of anchoring to nuclear structures (Agmon, Liefshitz, Zimmer, Fabre, & Kupiec, 2013; Dion, Kalck, Seeber, Schleker, & Gasser, 2013; Strecker et al., 2016).

Understanding the molecular mechanisms involved in the relocalization of DSBs in heterochromatin and other DNA sequences requires the ability to analyze the 4D dynamics of repair sites. This can be accomplished by live imaging of repair components, given that many repair factors form cytologically visible foci upon recruitment to DSBs (Costes, Chiolo, Pluth, Barcellos-Hoff, & Jakob, 2010; Delabaere et al., 2017; Haaf, Golub, Reddy, Radding, & Ward, 1995; Lisby, Barlow, Burgess, & Rothstein, 2004; Lisby & Rothstein, 2004; Liu, Li, Lee, & Maizels, 1999; Maser, Monsen, Nelms, & Petrini, 1997; Ryu et al., 2015; Scully et al., 1997). For example, the repair component Mu2/Mdc1 associates with the phosphorylated form of the histone variant H2Av (Chiolo et al., 2011; Dronamraju & Mason, 2009; Stucki et al., 2005) (γ H2Av, corresponding to mammalian γ H2AX (Fernandez-Capetillo, Lee, Nussenzweig, & Nussenzweig, 2004; Madigan, Chotkowski, & Glaser, 2002)), which marks DSBs, and mediates the recruitment of other HR proteins (Chapman & Jackson, 2008; Goldberg et al., 2003; Lou et al., 2006; Wang, Matsuoka, Carpenter, & Elledge, 2002). Thus, Mu2/Mdc1 foci can be used as a marker of repair sites throughout early and late steps of HR repair (Chiolo et al., 2011). ATRIP and TopBP1 are recruited to resected DSBs (Mordes, Glick, Zhao, & Cortez, 2008; Zou & Elledge, 2003); thus foci of these proteins mark resection (Chiolo et al., 2011). In late stages of HR, Rad51 promotes the search for a homologous template and strand invasion

(Sung, 1994), and Rad54 stabilizes Rad51-mediated strand invasion intermediates (Petukhova, Stratton, & Sung, 1998; Petukhova, Van Komen, Vergano, Klein, & Sung, 1999). GFP-tagging of these components can thus be used as a marker for later repair steps (Chiolo et al., 2011) (Fig. 1C).

To investigate the spatial and temporal dynamics of heterochromatin repair, mEGFP-tagged repair components are monitored relative to mCherry (mCh)-tagged HP1a as a marker for the heterochromatin domain. Early studies revealed that Mu2/Mdc1, ATRIP, and TopBP1 foci form inside the heterochromatin domain (Fig. 1D; Chiolo et al., 2011), while Rad51 and Rad54 foci form after relocalization (Chiolo et al., 2011). Repair foci leave the domain primarily between 10 and 30 min after DSB induction with ionizing radiation (IR) (Caridi et al., 2018; Chiolo et al., 2011; Ryu et al., 2016, 2015), and several foci reach the nuclear periphery in the first hour after IR (Caridi et al., 2018; Ryu et al., 2015) (Fig. 1E). Thus, investigating the 4D dynamics of heterochromatic repair foci requires live-cell imaging for at least 1 h after IR. A specific challenge of these studies is imaging the sample over long periods of time and with sufficient time points and Z-stacks to enable focus tracking, while limiting phototoxicity and photo-bleaching effects.

The use of *Drosophila* cultured cells greatly facilitates these experiments. In addition to the existence of a distinct heterochromatin domain, *Drosophila* cells are maintained at room temperature and ambient CO₂ concentrations (Cherbas & Gong, 2014), which minimizes stress from environmental changes during cell culturing, sample processing, and live imaging. Further, these cells are mostly in S and G2 phases of the cell cycle (Chiolo et al., 2011), which is ideal for studying HR repair. Finally, efficient RNAi procedures facilitate the investigation of the mechanisms involved in heterochromatin repair with genetic approaches (Zhou, Mohr, Hannon, & Perrimon, 2013).

Here, we describe a procedure for monitoring the spatial and temporal dynamics of heterochromatic DSBs in *Drosophila* cells following IR (Fig. 2), including: (i) the generation of stable cell lines expressing fluorescent-tagged repair and heterochromatin marks; (ii) a technique to image the same field before and after IR; (iii) the setup used to minimize light exposure with a DeltaVision deconvolution system (Applied Precision/GE Healthcare); and (iv) postimage processing done with SoftWorX (Applied Precision/GE Healthcare), which maximizes the recovery of information from low-exposure experiments while correcting for modest photobleaching. Additionally, we describe the workflow we implemented to track repair foci with

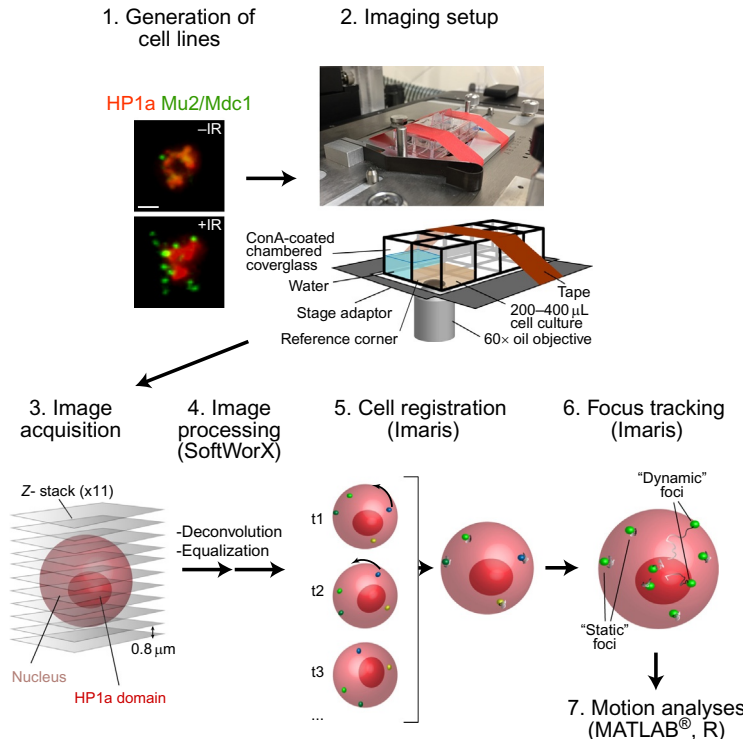
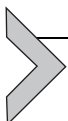


Fig. 2 Pipeline for image acquisition, processing, and analysis of focus dynamics in *Drosophila* heterochromatin. A stable cell line homogeneously expressing fluorescent-tagged protein (e.g., mCH-HP1a and mEGFP-Mu2/Mdc1) is placed in a well of a ConA-coated chambered coverslide, which is secured to the adaptor placed on the microscope stage. For long movies, evaporation of the media is limited by adding water to the surrounding wells. For tracking experiments, which require frequent imaging and long kinetics, photobleaching and phototoxicity are reduced by: (i) selecting bright fluorescent tags, which reduce the exposure time required to detect repair foci and heterochromatin; (ii) using the 2×2 binning option of the CoolsnapHQ2 camera, which dramatically increases the light collected by the camera per time unit; (iii) underexposing the sample and recovering most image details with postimage processing. Individual nuclei are registered with Imaris to correct for modest rotational and translational shifts, using “static” foci as a reference. “Dynamic” foci are then tracked using Imaris and the biophysical properties of the motion are characterized using customized scripts in MATLAB® and R.

Imaris (Bitplane) and derive mean square displacement (MSD) curves with a MATLAB® (Mathworks) script. Finally, we describe a new method we developed in R to identify directed motions within trajectories characterized by different types of motions. Together, these techniques enable

descriptive and quantitative analyses of the spatial and temporal dynamics of heterochromatin repair, which cannot be accomplished with fixed cell studies or biochemical approaches. Similar approaches have also broad applicability for the study of nuclear dynamics of repair foci in other contexts, from yeast to mammalian cells.



2. METHODS

Successful focus tracking and 4D analyses of focus motion over long-time periods require the optimization of different steps, including the selection of the brightest and most photoresistant fluorescent tags for live-cell imaging, the use of microscopes that mitigate the risk of cell damage, and the identification of imaging conditions and postimaging denoising approaches to recover image details while minimizing light exposure. Cell mobilization and nucleus registration approaches are also needed to isolate focus dynamics from cell dynamics. Once the positional data are collected, quantitative analyses enable the understanding of the biophysical properties of focus motion, including identifying directed motions.

2.1 Live-Cell Imaging of *Drosophila* Cells

2.1.1 Generation of Stable Cell Lines Expressing Fluorescent-Tagged Proteins

Live-cell imaging experiments greatly benefit from using stably transfected Kc167 (Kc) cells maintained as exponentially growing cultures. Kc cells are preferred over S2 cells because they adhere better to the substrate and maintain a more stable karyotype in the population. Live imaging and tracking experiments are facilitated by generating cell lines with homogeneous signals across the cell population, and a careful selection of tags for live imaging.

2.1.1.1 Cell Maintenance

Kc cells are maintained in Schneider's medium (Sigma) supplemented with 10% FBS (Gemini) and 2% Antibiotic-Antimycotic (Gibco) at 27°C. Schneider's media is an optimal choice for live imaging given the low autofluorescence. If cells are grown in media with high autofluorescence (e.g., SF-900 II, Gibco), we recommended shifting the cells to Schneider's media just before live cell imaging. Cells are kept in the exponential phase by splitting the culture every 3–5 days to maintain a concentration of $1.5\text{--}9 \times 10^6$ cells/mL. Cells do not grow equally well when seeded at a density below 1.5×10^5 cells/mL. For information about *Drosophila* cell

maintenance, see the *Drosophila* Genomics Resource Center (DGRC) website and [Yang and Reth \(2012\)](#).

2.1.1.2 Selecting Fluorescent Tags for Live-Cell Imaging

Live-cell imaging experiments are critically dependent on selecting the best combination of fluorescent tags for each protein of interest to maximize signal recovery during the entire kinetic. We have successfully used several fluorescent tags for live imaging of *Drosophila* cells (i.e., EGFP, GFP, mEGFP, mCitrin, mCerulean, mTurquoise2, mCherry, Aquamarine). However, mEGFP or EGFP tags' signals are among the brightest and most resistant to photobleaching and have been the best choice for 4D tracking of repair foci that requires frequent imaging over long periods of time ([Ryu et al., 2015](#)). mCherry (mCh) is also quite resistant to photobleaching and can be used to detect very abundant proteins or large nuclear structures in the same experiments, such as the heterochromatin domain (e.g., via expression of mCh-HP1a) or nuclear periphery components (e.g., via expression of mCh-LaminC) ([Chiolo et al., 2011](#); [Ryu et al., 2016, 2015](#)).

2.1.1.3 Generating Cell Lines That Express Tagged Proteins

Generating *Drosophila* cell lines that express fluorescent markers for DSB repair and heterochromatin is facilitated by using agents that deliver high transfection efficiency, like Cellfectin (Invitrogen), Transit-Insect (Mirus Bio LLC), Transit-2020 (Mirus Bio LLC), or Effectene (Qiagen) ([Fig. 3](#)). Transfections are done following manufacturer's procedures in six-well plates and typically using 2.5 µg of plasmids expressing each tagged protein of interest. Transfections with up to three plasmids result in most cells expressing all plasmids. For live imaging experiments requiring transient transfection, Cellfectin is preferred because it forms few if any precipitates during transfection. Transgene expression can be tested 3–4 days after transfection.

Using stable cell lines facilitates acquiring significantly more data in a short time, as every imaged field will contain ~20–50 transfected cells that can be analyzed for focus dynamics. Additionally, some repair components and nuclear architecture markers are not detectable after transient transfection, in which case stable cell lines are required. This needs to be empirically determined. To generate stable cell lines, 1 µg of plasmid carrying the selection cassette (i.e., pCoPuro ([Iwaki, Figuera, Ploplis, & Castellino, 2003](#)) or pCoHygro (Invitrogen)) is added to the plasmid mix during transfection, and cells are split in media containing the selection agent (i.e., 150 µg/mL

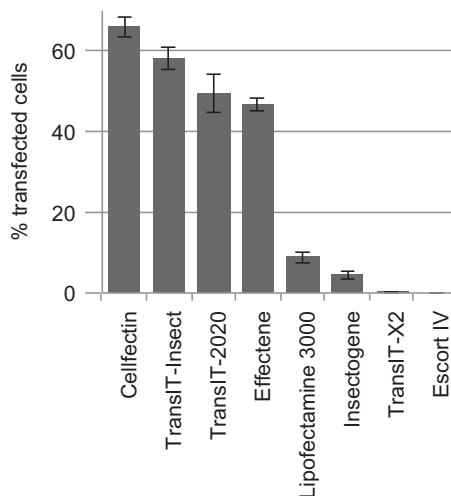


Fig. 3 High transfection efficiency is obtained with Cellfectin. High transfection efficiency facilitates the generation of stable Kc cell lines expressing fluorescent markers of the heterochromatin domain and damage foci. To optimize this step, different transfection agents were tested following manufacturers' instructions. Cells were transfected with 2.5 μ g of a midiprep of pCopia-mCh-HP1a, and the average number of cells expressing HP1a was estimated 72 h after transfection. The highest transfection efficiency obtained after several optimization steps is shown for each reagent, revealing the highest transfection efficiency using Cellfectin. Error bars show \pm SEM.

hygromycin or 300 μ g/mL puromycin) 3–5 days after transfection. For the following weeks, cells are split as needed to maintain them in the exponential growth phase, and recovery from the selection is typically observed after 4–5 weeks. Longer selection times render the signal more homogeneous across the culture but might also result in reduced signal intensity. Thus, for tracking experiments we recommend using the cells shortly after establishing a stable line.

Notes: We mostly use the Copia promoter to constitutively induce a protein of interest at low levels (typically similar to endogenous levels), although the metallothionein promoter (induced by CuSO₄) and the heat-shock promoter (induced by a 30-min temperature shift at 37°C) have also been used successfully. Given the potential effects of temperature shifts on gene expression, nuclear architecture, chromatin dynamics, or repair pathways (Li et al., 2015; Seong, Li, Shimizu, Nakamura, & Ishii, 2011; Velichko, Petrova, Kantidze, & Razin, 2012), and the potential secondary effects of expressing nonphysiological levels of the proteins, specific controls need to be applied when using these promoters. Additional considerations apply

to multicolor imaging. Imaging more than two channels increases the risk of phototoxicity and the time required for imaging each field. These might particularly affect tracking experiments, which require many time points and frequent imaging. Additionally, transfections with four plasmids (three plasmids expressing the tagged proteins plus the plasmid carrying a selection marker) are not very efficient, which complicates the generation of stable cell lines expressing all three fluorescent markers. If three-color imaging is required, it is recommended to express two (or three) of the tagged proteins in a multicistronic vector (Gonzalez et al., 2011). Alternatively, the selection marker can be cloned into one of the three vectors, or multiple tagged components can be integrated in the genome with sequential transfections.

2.1.2 *Immobilization of Cells for Microscopy*

A key step for 4D analysis of nuclear dynamics is immobilizing the cells on the substrate. This minimizes rotational and translational movements of the cells, reducing the need for postimaging corrections of the movement and dramatically improving the analysis of nuclear dynamics. We tested Concanavalin A (ConA) (Type VI or IV, Sigma), Polylysine (Sigma), and Cell-Tak (Corning), and found that ConA Type VI produces the best results.

Procedure for coverslide coating with ConA:

- 2.1.2.1** Prepare a solution of 1 mg/mL ConA in water. Stir for about 1 h, until mostly dissolved. Filter the solution with a 0.22- μ m pore-size filter.
- 2.1.2.2** Add \sim 100 μ L of ConA solution to each well of the eight-well chambered imaging coverslide (NuncTM Lab-TekTM II Chambered Coverglass, Thermo Scientific). The solution should form a thin layer coating the surface. Let the solution dry in the hood or in a 30°C incubator. For best results, repeat the coating two more times and use the coated coverslides within 1 week of preparation.

2.1.3 *Temperature Regulation During Live Imaging*

Maintaining a stable temperature while imaging is important to ensure consistency throughout the time course as well as across different experiments. To achieve stable temperature conditions, we use an environmental chamber mounted around the microscope that maintains the sample at 25°C during the experiment.

Note: For movies lasting a few hours, it is also important to limit evaporation of the growth media by adding water to empty wells surrounding the

well with the cells (Fig. 2). For even longer movies, it is helpful to place a slightly damp paper towel in the empty chambers to further limit evaporation.

2.1.4 Image Acquisition Setup With a DeltaVision Deconvolution Microscope

Depending on the proteins being analyzed and the microscope available, imaging parameters need to be empirically optimized to minimize photo-bleaching and phototoxicity. For imaging the dynamics of heterochromatic repair sites, we typically utilize cells stably expressing mCh-HP1a and a repair protein tagged with mEGFP (e.g., Mu2/Mdc1, ATRIP, or Rad51 (Caridi et al., 2018; Chiolo et al., 2011; Ryu et al., 2016, 2015)). The following procedure is optimized for cells expressing mCh-HP1a and mEGFP-Mu2/Mdc1 and imaging with a DeltaVision Elite deconvolution inverted microscope equipped with: white light LED (rated 100 Lumens at 350mA); seven-color InsightSSI solid-state illumination system; PlanApo 60 \times oil objective with N.A. 1.42; Ultimate Focus module; a Coolsnap HQ2 camera; and controlled by SoftWorX software (v. 6.1.3). The DeltaVision System is optimized for low-light imaging and image processing through deconvolution, which enables an excellent recovery of image details in underexposed samples (see Section 2.2.1). This makes this system an excellent choice for the experiments described here. Spinning disk microscopes or widefield microscopes used in combination with external image processing software have also been used successfully for similar experiments (see Hediger, Taddei, Neumann, & Gasser, 2004; Meister, Gehlen, Varela, Kalck, & Gasser, 2010 for an overview of different imaging technologies and Cho et al., 2014; Dimitrova, Chen, Spector, & de Lange, 2008; Dion et al., 2012; Lottersberger et al., 2015; Miné-Hattab & Rothstein, 2012; Su et al., 2015 for examples of their application to focus tracking experiments).

- 2.1.4.1** Split cells to a density of 2×10^6 cells/mL 48h before the experiment.
- 2.1.4.2** On the day of the experiment, transfer 200–400 μ L of cells into one well of the chambered coverslide, and let the cells settle for 10–15 min before imaging. Meanwhile, set the temperature of the environmental chamber of the microscope to 25°C.
- 2.1.4.3** On the microscope, manually position the 60 \times objective and the dichroic filter for GFP/mCh imaging.

- 2.1.4.4 Place immersion oil on the objective lens. Note that the immersion oil needs to be optimized based on objective, temperature conditions, and coverslip thickness to minimize spherical aberration while maximizing contrast in the images. With 1.5 mm chambered coverslide, we use an immersion oil refractive index = 1.512 (GE Healthcare Life Sciences). Follow the microscope manufacturer's instructions for this step.
- 2.1.4.5 Place the chambered coverslide on the stage adaptor. When imaging multiple fields, the movement of the stage can shift the coverglass on the stage adaptor, making it difficult to return to the same field of cells. To prevent this issue, secure the coverslide tightly using tape (Fig. 2) before placing it on the microscope stage. Adjust the stage level to bring the sample into focus.
- 2.1.4.6 In an effort to minimize light exposure during imaging, thus reducing photobleaching and phototoxicity, set the Coolsnap HQ2 camera at 2×2 binning. This results in less resolution but higher intensity collected per pixel. With this setting, we set an image size of 512×512 px, to collect the largest possible field of view.
- 2.1.4.7 Select the fields of interest. Illumination intensity is adjusted to the minimum level sufficient to see the sample, thus minimizing photobleaching of the signal while choosing the fields (e.g., 10% excitation intensity, or 10% T, for mCh and GFP). Suitable fields should contain an even distribution of cells as a monolayer, in addition to intense and homogeneous signals for mCh and GFP-tagged proteins. The number of fields that can be imaged in a single experiment is limited by the time required for imaging each field and the time interval between time points. We typically image four to five fields for each experiment. Once each field is selected, save its coordinates using “*Mark Point*” option in the “*Point List*” section in SoftWorx. The list of selected fields will appear in the “*Point List*” window.
- 2.1.4.8 Optimize the imaging path to visit all the fields using “*Optimize List*” followed by “*Compact List*” commands in the “*Point List*” section. This will minimize the time required to visit all of the selected fields, enabling imaging of more fields for each experiment.
- 2.1.4.9 Because cells are imaged before and after IR, it is essential to be able to return to the same fields after removing the chambered coverslide from the microscope for IR exposure. However, removal and repositioning of the sample might result in a slight shift

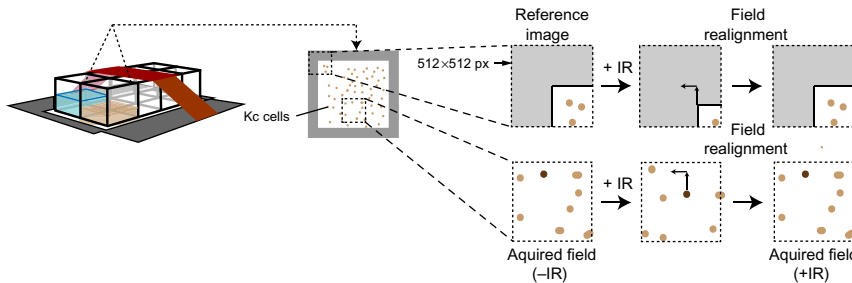


Fig. 4 Field realignment post IR. Focus tracking requires cell imaging before and after IR, but repositioning of the chambered coverslide on the stage after IR frequently results in a slight shift of the stage. This can be corrected using a reference field (e.g., a corner of the well). The reference field is manually recentered after IR, and the extent of correction applied enables determination of the *X* and *Y* shift. Corresponding corrections are applied to all fields of interest.

of the stage (Fig. 4). To identify the same field of cells, select a “landmark” field to use as a reference (such as a corner of the slide), and save its coordinates in addition to those of the selected fields of cells (Fig. 4).

- 2.1.4.10 Select the time of exposure for the sample based on the need to detect sufficient signal with the minimum exposure. For example, we use 10% T and a target intensity of 200 and 600 counts (approximately 5 and 15 ms) for mCh-HP1a and mEGFP-Mu2/Mdc1, respectively. This results in underexposing the image, but most image details can be recovered postimaging by optimized deconvolution and photobleaching correction algorithms available in SoftWorX (Fig. 5 and Section 2.2.1 of this protocol).
- 2.1.4.11 Adjust image acquisition settings to image the sample across its entire thickness with a minimum number of *Z*-stacks. This requires some optimization depending on the thickness of the sample. For *Drosophila* cells, image 11 *Z*-stacks at 0.8 μm distance between the *Z*-stacks. While a relatively high distance between *Z*-stacks reduces the resolution in this dimension, this is an excellent compromise between spatial resolution required for tracking and the need to minimize photobleaching and phototoxicity.
- 2.1.4.12 List the fields of interest (i.e., the points saved in the “*Point List*” section) in the “*Design/Run Experiment*,” “*Points*” tab, “*Visit Point List*” section. Activate the “*Ultimate Focus*” options with five

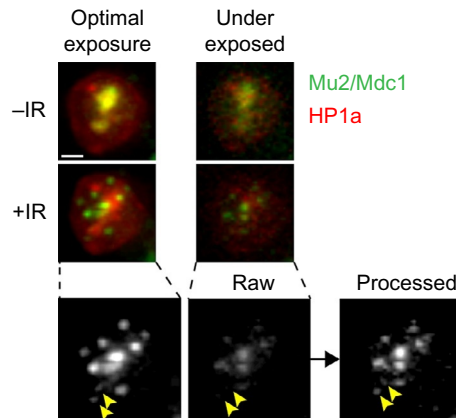


Fig. 5 Image details in underexposed samples are recovered with postimage processing. Underexposure of the cells enables the long and frequent image collection required for focus tracking while minimizing cell damage and photobleaching. The application of deconvolution and equalization algorithms enables the recovery of most details in underexposed images. In the example shown, a Kc cell stably expressing mEGFP-Mu2 and mCh-HP1a shows an overall enrichment of Mu2/Mdc1 signals inside the heterochromatin domain before IR (−IR), and damage foci associated with the heterochromatin domain at 10 min after IR (+IR) (Ryu et al., 2015). The signal has been collected first in underexposed conditions (5 ms for mCh and 20 ms for GFP, with 10% T), then in optimal imaging conditions (12 ms for mCh and 20 ms for GFP, with 100% T), for both time points as indicated. The noisy signal of raw underexposed images is significantly improved by postimage processing (deconvolution and equalization), revealing even the weak signals associated with small foci (arrowheads). Images are maximum intensity projections of one nucleus. Scale bar = 1 μ m.

iterations to assure that the cell focus is maintained throughout the experiment. This option corrects for axial drifts with an infrared laser-based system that detects the position of the coverslip relative to the sample. This is preferred over the “*Image-based autofocus before imaging*” option which causes photodamage while refocusing the image. If the “*Unlimited Focus*” module is not available on the system, manual adjustments of the focus or automated image-based autofocusing might be required throughout the kinetic.

2.1.4.13 Begin image capturing using “*Run*”–“*Start Scan*” (green arrowhead in the “*Design/Run Experiment*” window). The acquired image set corresponds to the “untreated” time point (−IR, Figs. 1–4).

2.1.4.14 Once all frames have been imaged, carefully remove the chambered coverslide without disturbing the stage position or the cells. Apply additional immersion oil onto the objective lens as needed.

2.1.5 *IR Treatment, Field Realignment, and Image Acquisition After IR*

This procedure enables the acquisition of several selected fields of cells after IR for each experiment, providing a large number of cells for analyses. Importantly, a direct investigation of cellular responses to IR requires the ability to image the same fields before and after IR, which is accomplished as described later.

2.1.5.1 We routinely expose the sample to 1.7 or 5 Gy IR, which corresponds to 14.5 or 44 s in our X-ray irradiator (X-RAD iR-160, Precision X-Ray, stage level 30), respectively. The timer is started half way through IR exposure. We use 5 Gy to track ATRIP foci (Ryu et al., 2015), and 1.7 Gy for Mu2/Mdc1 foci. Mu2/Mdc1 foci are typically more numerous than ATRIP foci, so reducing the intensity of IR minimizes overlapping signals (e.g., deriving from focus clustering; Chiolo et al., 2011, 2013), reducing the risk of ambiguous tracks. Notably, we did not detect major differences in MSD values between 1.7 and 5 Gy in our cells.

2.1.5.2 After exposure to IR, carefully place the chambered coverslide back on the microscope stage. Position the sample on the reference field (e.g., the corner of the chambered coverslide) using its saved coordinates (Fig. 4). Compare to the untreated images. If the stage shifted, move back the reference field until the original position and record the extent of the shift required for this realignment. Readjust the position of each field of cells accordingly. For example, if the reference field is shifted +300 μ m along the X-axis and +400 μ m along the Y-axis, move each field of cells –300 and –400 μ m along the X- and Y-axes, respectively, and save the new position (Fig. 4). For each field, also readjust the Z-axis to ensure that the sample is in focus and save the new position.

2.1.5.3 Adjust the “*Image Capturing*” parameters of the “*Experiment Setup*” option to collect images at 40 s time intervals for 1 h movies (91 images total). In SoftWorX, these options are under the “*Time-lapse*” tab in the “*Design/Run Experiment*” window. Click “*Start Scan*” to begin the imaging of the time points after IR (+IR, Fig. 2). Record the time point from IR at which the imaging starts (this is 3–5 min after IR in our experiments). Let the system acquire all the time points.

Notes: The imaging protocol described has been optimized for live imaging and tracking for MSD analysis of focus motion in response to IR. However, similar imaging approaches have broader applicability. For example, damage can be induced with hydroxyurea (1–2 mM) or methyl-methanesulfonate (0.0033%–0.1%). If cells are treated with chemicals, it is recommended to image untreated cells under control conditions to check for cellular toxicity coming from the solvent or imaging procedures. Longer movies are typically collected with longer time intervals between images to minimize photo-bleaching and phototoxicity. For example, we acquire images every 80 s for 2 h movies and every 30–60 min for 24 h movies. Finally, it is necessary to optimize imaging parameters (number of Z-stacks, intensity of light during exposure, frequency of time points) for each cell line, tagged component, and treatment. We recommend testing the effect of the imaging approach *per se* on DSB formation (e.g., Mu2/Mdc1 focus number (Caridi et al., 2018)) and cell ability to divide (e.g., by following the cell overnight and capturing cell division by imaging with 40-min time intervals (Chiolo et al., 2011)). Noninvasive imaging approaches should not interfere with cell division or induce DSB formation (Meister et al., 2010).

2.2 Image Processing and Focus Tracking

2.2.1 *Image Processing With SoftWorX*

The low light exposure conditions used in this protocol enable imaging over long time periods while limiting phototoxicity and photobleaching, but they also result in low signal-to-noise ratio in the collected images. A critical step in this analysis is the application of algorithms (deconvolution and equalization) that recover most image details postimaging, enabling precise identification and tracking of repair foci throughout the entire kinetic (Fig. 5). Equalization compensates for photobleaching effects by normalizing the signal intensity of each time point to a reference time point. This greatly facilitates automated detection and tracking of foci, which relies on the average signal intensity across the kinetic. Deconvolution is the mathematical correction of the distortion of an image resulting from diffraction and aberration of light passing through the optics of a microscope (Scalettar, Swedlow, Sedat, & Agard, 1996). This distortion can be quantified by establishing the shape of a single point object imaged with a microscope, or point spread function (PSF) (Scalettar et al., 1996). Deconvolution algorithms use the PSF to correct for the distortions, resulting in image deblurring, noise reduction, resolution improvement, and contrast enhancement (Scalettar et al., 1996). In addition to facilitating automated focus detection by increasing resolution, deconvolution corrects for image

distortions in the axial direction, dramatically reducing noise in the tracks coming from this dimension. In the DeltaVision microscope, equalization and deconvolution algorithms are fully integrated with the system and optimized for the specific microscope setup. However, similar results can be obtained with other software (e.g., Huygens Software Suite for deconvolution or Imaris for equalization).

- 2.2.1.1 Combine “-IR” and “+IR” files using the “*Image Fusion*” function in SoftWorX with the “*Combine time points for like wavelengths*” option.
- 2.2.2.1 Deconvolve the fused images in SoftWorX using five iterations of the “*Conservative*” protocol to improve contrast and resolution. In our experience, this is sufficient to improve image sharpness while limiting potential artifacts.
- 2.2.3.1 Correct the deconvolved file for modest photobleaching using the “*Equalize Time Points*” option.
- 2.2.4.1 Having individual cells cropped facilitates further image analysis with Imaris. For this purpose, crop selected cells using the “*Save File*” option in SoftWorX by selecting the field section of interest. Cells better suited for the registration step described next need to fit the following criteria: (i) the cell should appear nearly static throughout the kinetic; (ii) at least four “*static*” foci (i.e., foci that do not significantly move in the nucleus) are present throughout the kinetic (Fig. 2)—these will be used for registration; (iii) GFP and mCherry signals remain visible throughout the kinetics.

2.2.2 Cell Registration With Imaris

After cropping the selected cells, we utilize Imaris (v. 7.7.1 with XT module) to correct for minor cell/nucleus movement (“registration”) and to track foci for motion analysis. Registration is performed by tracking all of the foci (usually 4–12) that remain largely static throughout the kinetic and by correcting cell drift using those as a reference (Fig. 2). Using 7+ foci as a reference typically results in a better registration.

2.2.2.1 File Cropping

Remove the first time point (UNT) at this stage of the analysis by using the “*Crop Time*” function in Imaris. The first time point does not contain any IR-induced focus, so it cannot be used for registration. Save the cropped file with a new name to use this for further analysis. Keeping the original file is also important, as it contains information about which repair foci were

already present before IR. Those foci can be used for registration but not for tracking of IR-induced foci and MSD analyses.

2.2.2.2 Optional: Noise Reduction

Automatic focus tracking is greatly improved by reducing background signals and small focus vibrations along the Z-stack. Background signals are reduced using Imaris, by applying the “*Baseline Subtraction*” option in the “*Thresholding*” function of “*Image Processing*” to the channel with the foci. In addition, minor vibrations along the Z-stack are reduced by applying the “*Smooth Time*” function of “*Image Processing*” with a filter width of 1 to all time points. Together, these steps facilitate the subsequent automated tracking of foci.

2.2.2.3 Automated Focus Tracking

Focus tracking is done using the Imaris “*Spot Detection Tool*,” and the tracked foci are used to register the nucleus. Apply the following steps to generate the tracks, clicking the right pointing blue arrow to proceed through each step:

- i. Generate a new “*Spot*” in Imaris. Select the magic wand icon, and click on “*Rebuild*”;
- ii. Select the “*Track Spots Over Time*” box;
- iii. Select the “*Source Channel*” corresponding to the wavelength at which foci were imaged, using the dropdown menu;
- iv. In the “*Spot Detection*” section, select $0.2\text{ }\mu\text{m}$ as “*Estimated XY Diameter*.” This value reliably detects most DNA repair foci we examined. However, depending on the proteins being studied, this parameter may require empirical adjustments;
- v. The algorithm will place spheres corresponding to all detected foci. In the “*Filters*” section select “*Quality*.” Adjust the lowest threshold to a point at which the faintest foci are reliably distinguished from the background;
- vi. In the “*Add/Delete (Cursor Intersects with)*” section, using the dropdown menu, select the “*Specific Channel*” corresponding to the wavelength at which foci were imaged;
- vii. In the “*Algorithm*” section, select the “*Autoregressive Motion*.” In the “*Parameters*” section change the “*Max Distance*” to $0.5\text{ }\mu\text{m}$ and the “*Max Gap Size*” to 3. Check the box labeled “*Fill gaps with all detected objects*”;

viii. We apply two filters in the “*Classify Tracks*” section. Select “*Track Duration*” and adjust the lower threshold to eliminate tracks that only last a few time points. Add the “*Track Length*” filter and adjust the lower threshold to further remove short tracks. Click the right pointing orange double arrow icon to finalize the track detection.

2.2.2.4 Manual Editing of Tracks

Sometimes the tracks generated by Imaris include large jumps to unrelated foci, especially when those are in close spatial proximity relative to the focus of interest, in which case tracks detected automatically require manual adjustments. To edit a track, select the corresponding spot and the “*Edit Tracks*” icon. Select the time point that requires editing, delete it, manually recreate a new spot, and connect it to the preexistent track. Edit each track as necessary to assure that each focus is correctly identified throughout the kinetic.

2.2.2.5 Selection of Tracks for Registration

Identify foci that remain relatively stationary throughout the time course. These are typically euchromatic foci that originate outside the HP1a domain or foci that were already present in the nuclei before IR (e.g., spontaneous damage). We find that registration works better using at least seven foci, although four foci are sometimes sufficient. Foci characterized by extensive motion will affect the registration process and should be excluded at this stage.

2.2.2.6 Registration

Highlight all suitable tracks and click the “*Correct Drift*” button below the tracks window. In the “*Drift Correction Options*,” select “*Translational And Rotational Drift*.” For the “*Result Dataset Size*” select “*Include Entire Result*.” Confirm that the “*Correct objects’ positions*” box is selected. Then click “OK.” Imaris will register the nucleus based on the selected tracks, which will compensate for any minor translational and rotational motion of the nucleus during the experiment. Save the resulting file with a new name. This will be used for further focus tracking (Fig. 2).

2.2.3 Focus Tracking With Imaris

Tracking DNA damage foci is similar to the registration process, except that a new “spot” is generated for each tracked focus.

2.2.3.1 Optional

To minimize artificial vibrations of the nucleus resulting from the registration process, reapply the “Smooth time” function of “Image Processing” with a filter width of 1 to all the time points.

2.2.3.2 Focus Tracking

Visually identify a focus for tracking. Repeat steps 2.2.2.3 and 2.2.2.4, except that most tracks are filtered out using both upper and lower thresholds for “Quality” and “Track Duration” filters; only the focus of interest remains tracked. Repeat this step as many times as necessary to track all foci under investigation.

2.2.3.3 Nuclear Periphery Detection

The nuclear periphery is identified by creating a volume that corresponds to the diffuse nuclear signal generated by background mCh-HP1a or GFP-Mu2/Mdc1 signals. Using the “Automatic Creation” function, select the channel corresponding to HP1a or Mu2/Mdc1, and manually adjust smoothness and threshold to create a volume fitting the nuclear signal. Alternatively, a specific marker for the nuclear periphery (e.g., mCh-LaminC) can be used (Ryu et al., 2015).

2.2.4 4D Image Rendering

2.2.4.1 Optional

4D rendering of individual tracks can be done in Imaris to facilitate the analysis and display of each track (i.e., Fig. 1D). 4D rendering is obtained by generating a volume corresponding to the HP1a domain. Using the “Automatic Creation” function, select the channel corresponding to the HP1a domain and manually adjust smoothness and threshold to create a volume fitting the HP1a signal. The volume corresponding to the nuclear periphery (defined as described in Section 2.2.3.3) can be displayed at this step as well. Finally, select the focus track of interest, and deselect the green and red channels of the original image before saving the image.

2.3 Analysis of Focus Dynamics

2.3.1 Mean Square Displacement (MSD) Analysis

MSD analyses, which plot the average squared distance traveled by a focus at progressively increasing time intervals, provide quantitative measurements of the dynamic properties of focus motion (Dion & Gasser, 2013; Saxton & Jacobson, 1997; Spichal & Fabre, 2017). MSD values are

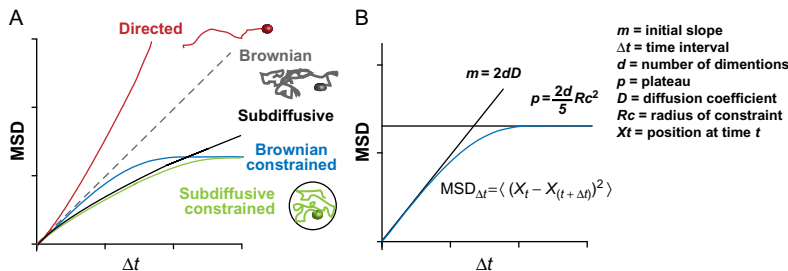


Fig. 6 MSD curves. MSD values are derived from the mean of the squared displacement calculated over increasing time intervals, Δt . (A) Examples of MSD plots corresponding to directed motion, Brownian motion, subdiffusive motion, and subdiffusive or Brownian motions via a constrained space are indicated. (B) For Brownian or subdiffusive motions, containment radius and diffusion coefficient are calculated using the plateau of the curve or the initial slope, as indicated (see text for details).

calculated at multiple time intervals to generate a curve for each track, and these curves are averaged to describe the behavior of a population of foci. The shape of the MSD curve reveals whether the motion of a particle is Brownian, subdiffusive or directed (Dion & Gasser, 2013; Saxton & Jacobson, 1997; Spichal & Fabre, 2017). MSD curves with increasing slope reflect DM, while linear MSD graphs indicate Brownian motion (Dion & Gasser, 2013; Meister et al., 2010; Saxton & Jacobson, 1997; Spichal & Fabre, 2017; Fig. 6A). However, given that the chromatin behaves as a polymer, and other constraints to the movement exist (e.g., chromatin compaction, molecular crowding, and anchoring to nuclear structures; reviewed in Dion & Gasser, 2013; Spichal & Fabre, 2017), chromatin motion is typically subdiffusive rather than Brownian, resulting in flattened MSD curves (Amitai, Seeber, Gasser, & Holcman, 2017; Marshall et al., 1997; Spichal & Fabre, 2017; Fig. 6A). In addition, subdiffusive (or Brownian) motion occurring in a constrained space (e.g., the nucleus or subnuclear domains) is characterized by MSD graphs that reach a plateau (Dion & Gasser, 2013; Saxton & Jacobson, 1997; Spichal & Fabre, 2017), and this is proportional to the radius of constraint (i.e., the radius of the volume explored by the focus; Fig. 6B). MSD curves enable calculating the radius of constraint and the diffusion coefficient as follows.

2.3.1.1 Extracting Positional Data

For each tracked spot, select the “Statistics” tab and click on the “Position” information in the dropdown menu of the “Detailed” tab. Click on the floppy disk icon to save the data as an excel file. The file contains

three columns: posX, posY, and posZ, corresponding to the coordinates of the focus at each time point. To use the MSD script provided as **Supplementary Information 1**: “MSD_script” (available on <https://doi.org/10.1016/bs.mie.2017.11.033>), add a column before those three and name it “t.” Number each time point with increasing number starting from “001” for the first time point, add the corresponding number at the beginning of each file name, and save this as a comma-separated values comma-separated values (.csv) file editable in Excel.

2.3.1.2 MSD Calculation

To derive MSD curves, positional data obtained from each track are processed with a MATLAB® script that generates MSD values for each focus. Open the MSD script in MATLAB® and point to the folder containing the .csv files in line 2 (e.g., “*myInputFolder*”). Enter the information of the destination folder in line 3 (e.g., “*myOutputFolder*”). Adjust the number of time points to be analyzed by editing the *timelapse_length* variable in line 8 (e.g., 92 time points in our experiments). This change will be reflected in the MSD table size and calculation. MSDs were calculated as described in [Dion and Gasser \(2013\)](#), [Meister et al. \(2010\)](#), [Miné-Hattab and Rothstein \(2012\)](#), and [Spichal and Fabre \(2017\)](#); for each position x_t (characterized by XYZ coordinates) at time t , and time interval Δt :

$$\text{MSD}_{\Delta t} = \left\langle (x_t - {}^t x_{(t + \Delta t)})^2 \right\rangle$$

Run the script. Output files will be saved in the destination folder. Note that multiple files (i.e., positional data from a large number of foci) can be read at once. As long as the file name is preceded by a progressively increasing number (i.e., 001, 002, etc.), the output will be a .csv file, with columns corresponding to MSD values for each focus and the focus number indicated at the bottom of each column. Rows correspond to increasing Δt (i.e., $\Delta t = 1$ in row 1, $\Delta t = 2$ in row 2, etc.). Combine all MSD data in one Excel file. Calculate and plot the average MSD value and standard errors.

2.3.1.3 Calculation of the Radius of Constraint and the Diffusion Coefficient for a Population of Foci

In order to calculate the plateau of the MSD curve, derive the curve that fits the data using MATLAB®’s “*curve fitting tools*” with this equation:

$$y = cst + A \left(1 - e^{-\frac{(x-x_f)}{\delta}} \right)$$

The plateau p of the curve, corresponding to $(p = cst + A)$, enables to calculate the radius of constraint Rc as:

$$Rc = \sqrt{5p/2d}$$

where d is the number of dimensions (three in this case). The diffusion coefficient D is derived from:

$$D = m/2d$$

where m is the initial slope of the MSD curve.

2.3.2 Detection of Directed Motions (DMs) in Mixed Trajectories

When DM occurs in a trajectory characterized by different types motion (e.g., preceded and/or followed by subdiffusive or constrained motions), also called mixed trajectory, an MSD analysis applied to the entire kinetic might mask the presence of DMs. This is even more likely when MSD values across different foci are averaged, using DMs initiated at different time points for each focus. Here we describe a method to identify time intervals characterized by DMs in these mixed trajectories, for each focus track. MSD curves for individual tracks are analyzed through a script in R ([Supplementary Information 2: “DM_script.R”](#) (available on <https://doi.org/10.1016/bs.mie.2017.11.033>) that returns the time intervals characterized by MSD graphs with increasing slope.

2.3.2.1 DM Identification

Open the script in R (<https://cran.r-project.org>) or R studio (<https://www.rstudio.com>) and point to the folder containing one of the .csv files obtained in [Section 2.3.1.1](#), in line 202 (i.e., “*list.files*”). The script derives MSD curves starting from each time point of the trajectory, and with progressively increasing Δt (with $\Delta t > 10$ time intervals). MSD curves are then smoothed using the *lowess* function with default parameters (<https://www.stat.ethz.ch/R-manual/R-devel/library/stats/html/lowess.html>) and segmented in two or more lines with increasing slopes. Points of slope change along the curve are detected using a *change point* analysis ([Zeileis, Kleiber, Krämer, & Hornik, 2003](#)) (*breakpoints* function with parameter *fraction* = 0.3; i.e., every regression fit must use at least 30% of the total data points). The ratio of slopes between two lines is used to identify DM, i.e., time intervals when the

MSD graph shows progressively increasing slopes. A few parameters can be modified to optimize the detection of DMs; the current values robustly detect DMs in our datasets, but adjustments might be required for different data:

- i. “*minratio*” is the minimum ratio between lines derived from MSD plots for considering the graph characterized by increasing slope, and the current value is set at 3.5. Higher values of *minratio* increase the stringency of detection of DMs (Note: a *minratio* higher than 2 is required to minimize the detection of false positives).
- ii. “*r2min*” is the minimum coefficient determination of the fitted line. This is set at 0.99 and higher values of this parameter increase the stringency of detection of DMs.
- iii. “*minslope*” is the minimum slope of the regression line at which data points are considered (current setting: 0.012). Lower values result in more foci with limited motions included in the analysis.

Run the script with the selected parameters. Time intervals characterized by DM appear in the “*Console*” work space and the corresponding graph is shown in the “*Plots*” section. If parameters are set correctly, those graphs show an upward curvature indicating DMs. The first and last time point of each time interval characterized by DM is saved in a file generated with file extension “.out” defined in the “*outsuffix*” variable and is shown as time intervals. Data are compiled to show the number and duration of DMs across the kinetics. Those typically correspond to time intervals characterized by DM in a mixed trajectory. The detection of time intervals characterized by DM can be validated by running the MSD script described in [Section 2.3.1](#) on the positional data corresponding to each time interval.

ACKNOWLEDGMENTS

This work was supported by NIH R21ES021541, NIH R01GM117376, the Mallinckrodt Foundation Award, and NSF Career 1751197 to I.C. We would like to thank S. Keagy for insightful comments on the chapter, B. Spatola for his help on an early version of the chapter, T. Nellimoottil for his help with the MSD script, T. Ryu for her analysis of Imaris filtering options and ConA optimization experiments, K. Chrzanowski for his input on Imaris tools, and the Chiolo Lab for helpful discussions. We also thank R. Rothstein, J. Miné-Hattab, and M. Smith for their input on data analyses.

DISCLOSURES

The authors have nothing to disclose.

REFERENCES

Agmon, N., Liefshitz, B., Zimmer, C., Fabre, E., & Kupiec, M. (2013). Effect of nuclear architecture on the efficiency of double-strand break repair. *Nature Cell Biology*, 15(6), 694–699. <https://doi.org/10.1038/ncb2745>.

Amaral, N., Ryu, T., Li, X., & Chiolo, I. (2017). Nuclear dynamics of heterochromatin repair. *Trends in Genetics*, 33(2), 86–100. <https://doi.org/10.1016/j.tig.2016.12.004>.

Amitai, A., Seeber, A., Gasser, S. M., & Holzman, D. (2017). Visualization of chromatin decompaction and break site extrusion as predicted by statistical polymer modeling of single-locus trajectories. *Cell Reports*, 18(5), 1200–1214. <https://doi.org/10.1016/j.celrep.2017.01.018>.

Ayoub, N., Jeyasekharan, A. D., Bernal, J. A., & Venkitaraman, A. R. (2008). HP1-beta mobilization promotes chromatin changes that initiate the DNA damage response. *Nature*, 453(7195), 682–686. <https://doi.org/10.1038/nature06875>.

Beucher, A., Birraux, J., Tchouandong, L., Barton, O., Shibata, A., Conrad, S., et al. (2009). ATM and Artemis promote homologous recombination of radiation-induced DNA double-strand breaks in G2. *The EMBO Journal*, 28(21), 3413–3427. <https://doi.org/10.1038/embj.2009.276>.

Burgess, R. C., Burman, B., Kruhlak, M. J., & Misteli, T. (2014). Activation of DNA damage response signaling by condensed chromatin. *Cell Reports*, 9(5), 1703–1717. <https://doi.org/10.1016/j.celrep.2014.10.060>.

Caridi, C., D'Agostino, C., Ryu, T., Zapotoczny, G., Li, X., Delabaere, L., et al. (2018). *Directed motions of heterochromatic DSBs require nuclear actin filaments and myosins*, Under revision.

Caridi, P. C., Delabaere, L., Zapotoczny, G., & Chiolo, I. (2017). And yet, it moves: Nuclear and chromatin dynamics of a heterochromatic double-strand break. *Philosophical Transactions of the Royal Society of London. Series B, Biological Sciences*, 372(1731), 20160291. <https://doi.org/10.1371/journal.pgen.1002473>.

Chapman, J. R., & Jackson, S. P. (2008). Phospho-dependent interactions between NBS1 and MDC1 mediate chromatin retention of the MRN complex at sites of DNA damage. *EMBO Reports*, 9(8), 795–801. <https://doi.org/10.1038/embor.2008.103>.

Cherbas, L., & Gong, L. (2014). Cell lines. *Methods*, 68(1), 74–81. <https://doi.org/10.1016/j.ymeth.2014.01.006>.

Chiolo, I., Minoda, A., Colmenares, S. U., Polyzos, A., Costes, S. V., & Karpen, G. H. (2011). Double-strand breaks in heterochromatin move outside of a dynamic HP1a domain to complete recombinational repair. *Cell*, 144(5), 732–744. <https://doi.org/10.1016/j.cell.2011.02.012>.

Chiolo, I., Tang, J., Georgescu, W., & Costes, S. V. (2013). Nuclear dynamics of radiation-induced foci in euchromatin and heterochromatin. *Mutation Research*, 750(1–2), 56–66. <https://doi.org/10.1016/j.mrfmmm.2013.08.001>.

Cho, N. W., Dilley, R. L., Lampson, M. A., & Greenberg, R. A. (2014). Interchromosomal homology searches drive directional ALT telomere movement and synapsis. *Cell*, 159(1), 108–121. <https://doi.org/10.1016/j.cell.2014.08.030>.

Chung, D. K., Chan, J. N., Strecker, J., Zhang, W., Ebrahimi-Ardebili, S., Lu, T., et al. (2015). Perinuclear tethers license telomeric DSBs for a broad kinesin- and NPC-dependent DNA repair process. *Nature Communications*, 6, 7742. <https://doi.org/10.1038/ncomms8742>.

Churikov, D., Charifi, F., Eckert-Boulet, N., Silva, S., Simon, M. N., Lisby, M., et al. (2016). SUMO-dependent relocation of eroded telomeres to nuclear pore complexes controls telomere recombination. *Cell Reports*, 15(6), 1242–1253. <https://doi.org/10.1016/j.celrep.2016.04.008>.

Costes, S. V., Chiolo, I., Pluth, J. M., Barcellos-Hoff, M. H., & Jakob, B. (2010). Spatio-temporal characterization of ionizing radiation induced DNA damage foci and their relation to chromatin organization. *Mutation Research*, 704(1–3), 78–87. <https://doi.org/10.1016/j.mrrev.2009.12.006>.

Delabaeke, L., & Chiolo, I. (2016). ReiNF4rcing repair pathway choice during cell cycle. *Cell Cycle*, 15(9), 1182–1183. <https://doi.org/10.1080/15384101.2016.1159108>.

Delabaeke, L., Ertl, H. A., Massey, D. J., Hofley, C. M., Sohail, F., Bienenstock, E. J., et al. (2017). Aging impairs double-strand break repair by homologous recombination in *Drosophila* germ cells. *Aging Cell*, 16, 320–328. <https://doi.org/10.1111/acel.12556>.

Dimitrova, N., Chen, Y. C., Spector, D. L., & de Lange, T. (2008). 53BP1 promotes non-homologous end joining of telomeres by increasing chromatin mobility. *Nature*, 456(7221), 524–528. <https://doi.org/10.1038/nature07433>.

Dion, V., & Gasser, S. M. (2013). Chromatin movement in the maintenance of genome stability. *Cell*, 152(6), 1355–1364. <https://doi.org/10.1016/j.cell.2013.02.010>.

Dion, V., Kalck, V., Horigome, C., Towbin, B. D., & Gasser, S. M. (2012). Increased mobility of double-strand breaks requires Mec1, Rad9 and the homologous recombination machinery. *Nature Cell Biology*, 14(5), 502–509. <https://doi.org/10.1038/ncb2465>.

Dion, V., Kalck, V., Seeber, A., Schleker, T., & Gasser, S. M. (2013). Cohesin and the nucleolus constrain the mobility of spontaneous repair foci. *EMBO Reports*, 14(11), 984–991. <https://doi.org/10.1038/embor.2013.142>.

Dronamraju, R., & Mason, J. M. (2009). Recognition of double strand breaks by a mutator protein (MU2) in *Drosophila melanogaster*. *PLoS Genetics*, 5(5), e1000473. <https://doi.org/10.1371/journal.pgen.1000473>.

Fernandez-Capetillo, O., Lee, A., Nussenzweig, M., & Nussenzweig, A. (2004). H2AX: The histone guardian of the genome. *DNA Repair (Amst)*, 3(8–9), 959–967. <https://doi.org/10.1016/j.dnarep.2004.03.024>.

Goldberg, M., Stucki, M., Falck, J., D'Amours, D., Rahman, D., Pappin, D., et al. (2003). MDC1 is required for the intra-S-phase DNA damage checkpoint. *Nature*, 421(6926), 952–956. <https://doi.org/10.1038/nature01445>.

Gonzalez, M., Martin-Ruiz, I., Jimenez, S., Pirone, L., Barrio, R., & Sutherland, J. D. (2011). Generation of stable *Drosophila* cell lines using multicistronic vectors. *Scientific Reports*, 1, 75. <https://doi.org/10.1038/srep00075>.

Haaf, T., Golub, E. I., Reddy, G., Radding, C. M., & Ward, D. C. (1995). Nuclear foci of mammalian Rad51 recombination protein in somatic cells after DNA damage and its localization in synaptonemal complexes. *Proceedings of the National Academy of Sciences of the United States of America*, 92(6), 2298–2302.

Hauer, M. H., Seeber, A., Singh, V., Thierry, R., Sack, R., Amitai, A., et al. (2017). Histone degradation in response to DNA damage enhances chromatin dynamics and recombination rates. *Nature Structural & Molecular Biology*, 24(2), 99–107. <https://doi.org/10.1038/nsmb.3347>.

Hediger, F., Taddei, A., Neumann, F. R., & Gasser, S. M. (2004). Methods for visualizing chromatin dynamics in living yeast. *Methods in Enzymology*, 375, 345–365.

Ho, J. W., Jung, Y. L., Liu, T., Alver, B. H., Lee, S., Ikegami, K., et al. (2014). Comparative analysis of metazoan chromatin organization. *Nature*, 512(7515), 449–452. <https://doi.org/10.1038/nature13415>.

Horigome, C., Bustard, D. E., Marcomini, I., Delgoshai, N., Tsai-Pflugfelder, M., Cobb, J. A., et al. (2016). PolySUMOylation by Siz2 and Mms21 triggers relocation of DNA breaks to nuclear pores through the Slx5/Slx8 STUbL. *Genes & Development*, 30(8), 931–945. <https://doi.org/10.1101/gad.277665.116>.

Horigome, C., Oma, Y., Konishi, T., Schmid, R., Marcomini, I., Hauer, M. H., et al. (2014). SWR1 and INO80 chromatin remodelers contribute to DNA double-strand

break perinuclear anchorage site choice. *Molecular Cell*, 55(4), 626–639. <https://doi.org/10.1016/j.molcel.2014.06.027>.

Hoskins, R. A., Carlson, J. W., Kennedy, C., Acevedo, D., Evans-Holm, M., Frise, E., et al. (2007). Sequence finishing and mapping of *Drosophila melanogaster* heterochromatin. *Science*, 316(5831), 1625–1628. <https://doi.org/10.1126/science.1139816>.

Hoskins, R. A., Carlson, J. W., Wan, K. H., Park, S., Mendez, I., Galle, S. E., et al. (2015). The release 6 reference sequence of the *Drosophila melanogaster* genome. *Genome Research*, 25(3), 445–458. <https://doi.org/10.1101/gr.185579.114>.

Iwaki, T., Figuera, M., Ploplis, V. A., & Castellino, F. J. (2003). Rapid selection of *Drosophila* S2 cells with the puromycin resistance gene. *BioTechniques*, 35(3), 482–484, 486.

Jakob, B., Splinter, J., Conrad, S., Voss, K. O., Zink, D., Durante, M., et al. (2011). DNA double-strand breaks in heterochromatin elicit fast repair protein recruitment, histone H2AX phosphorylation and relocation to euchromatin. *Nucleic Acids Research*, 39(15), 6489–6499. <https://doi.org/10.1093/nar/gkr230>.

Janssen, A., Breuer, G. A., Brinkman, E. K., van der Meulen, A. I., Borden, S. V., van Steensel, B., et al. (2016). A single double-strand break system reveals repair dynamics and mechanisms in heterochromatin and euchromatin. *Genes & Development*, 30(14), 1645–1657. <https://doi.org/10.1101/gad.283028.116>.

Kalocsay, M., Hiller, N. J., & Jentsch, S. (2009). Chromosome-wide Rad51 spreading and SUMO-H2A.Z-dependent chromosome fixation in response to a persistent DNA double-strand break. *Molecular Cell*, 33(3), 335–343. <https://doi.org/10.1016/j.molcel.2009.01.016>.

Khadaroo, B., Teixeira, M. T., Luciano, P., Eckert-Boulet, N., Germann, S. M., Simon, M. N., et al. (2009). The DNA damage response at eroded telomeres and tethering to the nuclear pore complex. *Nature Cell Biology*, 11(8), 980–987. <https://doi.org/10.1038/ncb1910>.

Krawczyk, P. M., Borovski, T., Stap, J., Cijssouw, T., ten Cate, R., Medema, J. P., et al. (2012). Chromatin mobility is increased at sites of DNA double-strand breaks. *Journal of Cell Science*, 125(Pt. 9), 2127–2133. <https://doi.org/10.1242/jcs.089847>.

Kruhlak, M. J., Celeste, A., Dellaire, G., Fernandez-Capetillo, O., Müller, W. G., McNally, J. G., et al. (2006). Changes in chromatin structure and mobility in living cells at sites of DNA double-strand breaks. *The Journal of Cell Biology*, 172(6), 823–834.

Li, L., Lyu, X., Hou, C., Takenaka, N., Nguyen, H. Q., Ong, C. T., et al. (2015). Widespread rearrangement of 3D chromatin organization underlies polycomb-mediated stress-induced silencing. *Molecular Cell*, 58(2), 216–231. <https://doi.org/10.1016/j.molcel.2015.02.023>.

Lisby, M., Barlow, J. H., Burgess, R. C., & Rothstein, R. (2004). Choreography of the DNA damage response: Spatiotemporal relationships among checkpoint and repair proteins. *Cell*, 118(6), 699–713.

Lisby, M., & Rothstein, R. (2004). DNA damage checkpoint and repair centers. *Current Opinion in Cell Biology*, 16(3), 328–334. <https://doi.org/10.1016/j.ceb.2004.03.011>.

Liu, Y., Li, M., Lee, E. Y., & Maizels, N. (1999). Localization and dynamic relocalization of mammalian Rad52 during the cell cycle and in response to DNA damage. *Current Biology*, 9(17), 975–978.

Lottersberger, F., Karssemeijer, R. A., Dimitrova, N., & de Lange, T. (2015). 53BP1 and the LINC complex promote microtubule-dependent DSB mobility and DNA repair. *Cell*, 163(4), 880–893. <https://doi.org/10.1016/j.cell.2015.09.057>.

Lou, Z., Minter-Dykhouse, K., Franco, S., Gostissa, M., Rivera, M. A., Celeste, A., et al. (2006). MDC1 maintains genomic stability by participating in the amplification of ATM-dependent DNA damage signals. *Molecular Cell*, 21(2), 187–200. <https://doi.org/10.1016/j.molcel.2005.11.025>.

Madigan, J. P., Chotkowski, H. L., & Glaser, R. L. (2002). DNA double-strand break-induced phosphorylation of *Drosophila* histone variant H2Av helps prevent radiation-induced apoptosis. *Nucleic Acids Research*, 30(17), 3698–3705.

Marshall, W. F., Straight, A., Marko, J. F., Swedlow, J., Dernburg, A., Belmont, A., et al. (1997). Interphase chromosomes undergo constrained diffusional motion in living cells. *Current Biology*, 7(12), 930–939.

Maser, R. S., Monsen, K. J., Nelms, B. E., & Petrini, J. H. (1997). hMre11 and hRad50 nuclear foci are induced during the normal cellular response to DNA double-strand breaks. *Molecular and Cellular Biology*, 17(10), 6087–6096.

Meister, P., Gehlen, L. R., Varela, E., Kalck, V., & Gasser, S. M. (2010). Visualizing yeast chromosomes and nuclear architecture. *Methods in Enzymology*, 470, 535–567. [https://doi.org/10.1016/S0076-6879\(10\)70021-5](https://doi.org/10.1016/S0076-6879(10)70021-5).

Miné-Hattab, J., & Rothstein, R. (2012). Increased chromosome mobility facilitates homology search during recombination. *Nature Cell Biology*, 14(5), 510–517. <https://doi.org/10.1038/ncb2472>.

Mordes, D. A., Glick, G. G., Zhao, R., & Cortez, D. (2008). TopBP1 activates ATR through ATRIP and a PIKK regulatory domain. *Genes & Development*, 22(11), 1478–1489. <https://doi.org/10.1101/gad.1666208>.

Nagai, S., Dubrana, K., Tsai-Pflugfelder, M., Davidson, M. B., Roberts, T. M., Brown, G. W., et al. (2008). Functional targeting of DNA damage to a nuclear pore-associated SUMO-dependent ubiquitin ligase. *Science*, 322(5901), 597–602. <https://doi.org/10.1126/science.1162790>.

Neumann, F. R., Dion, V., Gehlen, L. R., Tsai-Pflugfelder, M., Schmid, R., Taddei, A., et al. (2012). Targeted INO80 enhances subnuclear chromatin movement and ectopic homologous recombination. *Genes & Development*, 26(4), 369–383. <https://doi.org/10.1101/gad.176156.111>.

Oza, P., Jaspersen, S. L., Miele, A., Dekker, J., & Peterson, C. L. (2009). Mechanisms that regulate localization of a DNA double-strand break to the nuclear periphery. *Genes & Development*, 23(8), 912–927. <https://doi.org/10.1101/gad.1782209>.

Peng, J. C., & Karpen, G. H. (2008). Epigenetic regulation of heterochromatic DNA stability. *Current Opinion in Genetics & Development*, 18(2), 204–211. <https://doi.org/10.1016/j.gde.2008.01.021>.

Petukhova, G., Stratton, S., & Sung, P. (1998). Catalysis of homologous DNA pairing by yeast Rad51 and Rad54 proteins. *Nature*, 393(6680), 91–94. <https://doi.org/10.1038/30037>.

Petukhova, G., Van Komen, S., Vergano, S., Klein, H., & Sung, P. (1999). Yeast Rad54 promotes Rad51-dependent homologous DNA pairing via ATP hydrolysis-driven change in DNA double helix conformation. *The Journal of Biological Chemistry*, 274(41), 29453–29462.

Riddle, N. C., Minoda, A., Kharchenko, P. V., Alekseyenko, A. A., Schwartz, Y. B., Tolstorukov, M. Y., et al. (2011). Plasticity in patterns of histone modifications and chromosomal proteins in *Drosophila* heterochromatin. *Genome Research*, 21(2), 147–163. <https://doi.org/10.1101/gr.110098.110>.

Ryu, T., Bonner, M. R., & Chiolo, I. (2016). Cervantes and Quijote protect heterochromatin from aberrant recombination and lead the way to the nuclear periphery. *Nucleus*, 7(5), 485–497. <https://doi.org/10.1080/19491034.2016.1239683>.

Ryu, T., Spatola, B., Delabaere, L., Bowlin, K., Hopp, H., Kunitake, R., et al. (2015). Heterochromatic breaks move to the nuclear periphery to continue recombinational repair. *Nature Cell Biology*, 17(11), 1401–1411. <https://doi.org/10.1038/ncb3258>.

Saad, H., Gallardo, F., Dalvai, M., Tanguy-le-Gac, N., Lane, D., & Bystricky, K. (2014). DNA dynamics during early double-strand break processing revealed by non-intrusive

imaging of living cells. *PLoS Genetics*, 10(3), e1004187. <https://doi.org/10.1371/journal.pgen.1004187>.

Saxton, M. J., & Jacobson, K. (1997). Single-particle tracking: Applications to membrane dynamics. *Annual Review of Biophysics and Biomolecular Structure*, 26, 373–399. <https://doi.org/10.1146/annurev.biophys.26.1.373>.

Scalettar, B. A., Swedlow, J. R., Sedat, J. W., & Agard, D. A. (1996). Dispersion, aberration and deconvolution in multi-wavelength fluorescence images. *Journal of Microscopy*, 182(Pt. 1), 50–60.

Scully, R., Chen, J., Ochs, R. L., Keegan, K., Hoekstra, M., Feunteun, J., et al. (1997). Dynamic changes of BRCA1 subnuclear location and phosphorylation state are initiated by DNA damage. *Cell*, 90(3), 425–435.

Seeber, A., Dion, V., & Gasser, S. M. (2013). Checkpoint kinases and the INO80 nucleosome remodeling complex enhance global chromatin mobility in response to DNA damage. *Genes & Development*, 27(18), 1999–2008. <https://doi.org/10.1101/gad.222992.113>.

Seong, K. H., Li, D., Shimizu, H., Nakamura, R., & Ishii, S. (2011). Inheritance of stress-induced, ATF-2-dependent epigenetic change. *Cell*, 145(7), 1049–1061. <https://doi.org/10.1016/j.cell.2011.05.029>.

Spichal, M., Brion, A., Herbert, S., Cournac, A., Marbouth, M., Zimmer, C., et al. (2016). Evidence for a dual role of actin in regulating chromosome organization and dynamics in yeast. *Journal of Cell Science*, 129(4), 681–692. <https://doi.org/10.1242/jcs.175745>.

Spichal, M., & Fabre, E. (2017). The emerging role of the cytoskeleton in chromosome dynamics. *Frontiers in Genetics*, 8, 60. <https://doi.org/10.3389/fgene.2017.00060>.

Strecker, J., Gupta, G. D., Zhang, W., Bashkurov, M., Landry, M. C., Pelletier, L., et al. (2016). DNA damage signalling targets the kinetochore to promote chromatin mobility. *Nature Cell Biology*, 18(3), 281–290. <https://doi.org/10.1038/ncb3308>.

Stucki, M., Clapperton, J. A., Mohammad, D., Yaffe, M. B., Smerdon, S. J., & Jackson, S. P. (2005). MDC1 directly binds phosphorylated histone H2AX to regulate cellular responses to DNA double-strand breaks. *Cell*, 123(7), 1213–1226. <https://doi.org/10.1016/j.cell.2005.09.038>.

Su, X. A., Dion, V., Gasser, S. M., & Freudenreich, C. H. (2015). Regulation of recombination at yeast nuclear pores controls repair and triplet repeat stability. *Genes & Development*, 29(10), 1006–1017. <https://doi.org/10.1101/gad.256404.114>.

Sung, P. (1994). Catalysis of ATP-dependent homologous DNA pairing and strand exchange by yeast RAD51 protein. *Science*, 265(5176), 1241–1243.

Swartz, R. K., Rodriguez, E. C., & King, M. C. (2014). A role for nuclear envelope-bridging complexes in homology-directed repair. *Molecular Biology of the Cell*, 25(16), 2461–2471. <https://doi.org/10.1091/mbc.E13-10-0569>.

Therizols, P., Fairhead, C., Cabal, G. G., Genovesio, A., Olivo-Marin, J. C., Dujon, B., et al. (2006). Telomere tethering at the nuclear periphery is essential for efficient DNA double strand break repair in subtelomeric region. *The Journal of Cell Biology*, 172(2), 189–199. <https://doi.org/10.1083/jcb.200505159>.

Torres-Rosell, J., Sunjavaric, I., De Piccoli, G., Sacher, M., Eckert-Boulet, N., Reid, R., et al. (2007). The Smc5-Smc6 complex and SUMO modification of Rad52 regulates recombinational repair at the ribosomal gene locus. *Nature Cell Biology*, 9(8), 923–931.

Tsouroula, K., Furst, A., Rogier, M., Heyer, V., Maglott-Roth, A., Ferrand, A., et al. (2016). Temporal and spatial uncoupling of DNA double strand break repair pathways within mammalian heterochromatin. *Molecular Cell*, 63(2), 293–305. <https://doi.org/10.1016/j.molcel.2016.06.002>.

van Sluis, M., & McStay, B. (2015). A localized nucleolar DNA damage response facilitates recruitment of the homology-directed repair machinery independent of cell cycle stage. *Genes & Development*, 29(11), 1151–1163. <https://doi.org/10.1101/gad.260703.115>.

Velichko, A. K., Petrova, N. V., Kantidze, O. L., & Razin, S. V. (2012). Dual effect of heat shock on DNA replication and genome integrity. *Molecular Biology of the Cell*, 23(17), 3450–3460. <https://doi.org/10.1091/mbc.E11-12-1009>.

Wang, B., Matsuoka, S., Carpenter, P. B., & Elledge, S. J. (2002). 53BP1, a mediator of the DNA damage checkpoint. *Science*, 298(5597), 1435–1438. <https://doi.org/10.1126/science.1076182>.

Yang, J., & Reth, M. (2012). Drosophila S2 Schneider cells: A useful tool for rebuilding and redesigning approaches in synthetic biology. *Methods in Molecular Biology*, 813, 331–341. https://doi.org/10.1007/978-1-61779-412-4_20.

Zeileis, A., Kleiber, C., Krämer, W., & Hornik, K. (2003). Testing and dating of structural changes in practice. *Computational Statistics and Data Analysis*, 44, 109–123.

Zhou, R., Mohr, S., Hannon, G. J., & Perrimon, N. (2013). Inducing RNAi in Drosophila cells by transfection with dsRNA. *Cold Spring Harbor Protocols*, 2013(5), 461–463. <https://doi.org/10.1101/pdb.prot074351>.

Ziv, Y., Bielopolski, D., Galanty, Y., Lukas, C., Taya, Y., Schultz, D. C., et al. (2006). Chromatin relaxation in response to DNA double-strand breaks is modulated by a novel ATM- and KAP-1 dependent pathway. *Nature Cell Biology*, 8(8), 870–876. <https://doi.org/10.1038/ncb1446>.

Zou, L., & Elledge, S. J. (2003). Sensing DNA damage through ATRIP recognition of RPA-ssDNA complexes. *Science*, 300(5625), 1542–1548. <https://doi.org/10.1126/science.1083430>.